PHYSICAL REVIEW B **89**, 104104 (2014)

Non-180° polarization rotation of ferroelectric $(Bi_{0.5}Na_{0.5})TiO_3$ single crystals under electric field

Yuuki Kitanaka,[1] Ken Yanai,[1] Yuji Noguchi,[1] Masaru Miyayama,[1] Yutaka Kagawa,[1]
Chikako Moriyoshi,[2] and Yoshihiro Kuroiwa[2]
[1]*Research Center for Advanced Science and Technology, The University of Tokyo, 4-6-1 Komaba, Meguro, Tokyo 153-8904, Japan*
[2]*Graduate School of Science, Hiroshima University, 1-3-1 Kagamiyama, Higashihiroshima, Hiroshima 739-8526, Japan*

(Received 8 January 2014; revised manuscript received 24 January 2014; published 10 March 2014)

The behavior of the polarization switching by applying electric fields (E) along the ⟨100⟩ and ⟨111⟩ directions has been investigated for the single crystals of ferroelectric $(Bi_{0.5}Na_{0.5})TiO_3$ (BNT) using high-energy synchrotron radiation x-ray diffraction (SR-XRD) and density functional theory (DFT) calculations. Single-crystal SR-XRD analyses reveal that the E-induced switching of spontaneous polarization (P_s) occurs via the non-180° (71° and/or 109°) P_s rotation. The DFT calculations show that the energy barrier for the 71° P_s rotation is much lower than those for the 109° P_s rotation and for the direct 180° P_s reversal. These experimental and DFT calculation results lead to the conclusion that the 71° P_s rotation is the dominant pathway for the E-induced polarization switching in the BNT crystals.

DOI: 10.1103/PhysRevB.89.104104 PACS number(s): 77.80.Fm, 77.84.Cg, 61.05.cp, 71.15.−m

I. INTRODUCTION

The dynamics of domain structures under electric fields in ferroelectrics are the underlying basis of various functionalities, such as dielectricity, piezoelectricity, electro-optic effects, and polarization switching. Since the performance of ferroelectric devices is governed not only by intrinsic lattice deformations but also by the domain dynamics, experimental and calculation studies have been extensively performed to elucidate the dynamic behavior of domain structures. The engineering of non-180° ferroelastic domains has attracted much attention as a promising approach for enhancing the functional properties of perovskite ferroelectrics [1–6]. Tetragonal $BaTiO_3$ crystals with a 90°-domain structure have been reported to show superior dielectric and piezoelectric properties compared with the single-domain crystals [3,4]. The 71° and 109° domain walls (DWs) in rhombohedral $BiFeO_3$ thin films have been found to yield a steady-state photovoltaic current under light illuminations [5,6]. The physics of the ferroelectric domains and their dynamics under electric fields (E) are of great interest from both fundamental and technological viewpoints.

Due to the recent developments in atomic-scale microscopy and theoretical calculations, there have been significant advances in understanding the detailed structures of DWs and the dynamic features of domain structures in ferroelectrics [7,8]. High-resolution electron microscopy has revealed the distribution of the ferroelectric displacements of constituent atoms in the vicinity of DWs, elucidating the atomic-scale structures of the DWs such as their strain fields [9]. Phase-field simulations based on the Landau-Ginzburg-Devonshire (LGD) theory provide a clear picture of the static and dynamic domain behavior in perovskite ferroelectrics [10,11]. Almost all these studies, however, have focused only on the spontaneous polarization (P_s) and strain originating directly from the atomic displacements along the polar axis. Some perovskite ferroelectrics contain nonpolar atomic displacements due to antiferrodistortive instabilities in addition to the P_s-derived polar strain [12–15]. In bismuth layer-structured ferroelectrics, nonpolar octahedral rotations around the crystallographic a axis have much larger structural distortions compared with the cooperative ferroelectric displacements along the a axis [16,17]. For some hexagonal manganite multiferroics, a nonpolar distortion with a double-well energy potential that constitutes the primarily order parameter induces a ferroelectric polarization with a single-well potential [18]. This nonpolar component has been reported to make a remarkable impact on the electric properties along with an unusual configuration of ferroelectric domains [19]. These nonpolar distortions derived from the condensation of zone-boundary phonon modes more or less influence the behavior of ferroelectric domains [19,20], but these influences have not been thoroughly clarified yet due to a lack of experimental data and theoretical calculations.

In this paper, the dynamic behavior of domain structures in a ferroelectric crystal having both nonpolar and polar distortions is investigated by using single-crystal x-ray diffraction analyses and density functional theory (DFT) calculations. Bismuth sodium titanate $(Bi_{0.5}Na_{0.5})TiO_3$ (BNT) [21] is selected as a model ferroelectric material, because BNT has the large structural distortions of the nonpolar and polar components, in which the atomic displacements of the nonpolar TiO_6 octahedral tilting are comparable to those of the ferroelectric polarization [22]. High-quality BNT single crystals grown by the high-oxygen pressure crystal growth method [23,24] are used for the diffraction and polarization-hysteresis measurements. High-energy synchrotron radiation x-ray diffraction (SR-XRD) measurements adapted in this study enable us to obtain information of the domain structures inside the crystals during polarization switching under electric fields. The energy barriers for the polarization switching are estimated by the DFT calculations in which the possible changes in the direction of the TiO_6 rotation accompanied by the reversal of the P_s vector are taken into consideration.

II. EXPERIMENTAL PROCEDURE

Single crystals of BNT were grown at a high oxygen pressure of 0.9–1.0 MPa by a flux method [23] and a top-seeded solution growth method [24]. We have reported in our previous works that the high-oxygen-pressure atmosphere greatly suppresses the formation of the vacancies of bismuth and oxygen at high temperatures [23–26]. For the high-quality crystals grown by our technique, the P_s vector is completely reversed by applying an E of above ~50 kV/cm [26,27]. The details of the crystal growth are described in Refs. [23,24].

For the SR-XRD measurements, the crystals were cut into plates with a thickness of 0.2 mm, and then gold electrodes 20 nm in thickness were sputtered onto the cut surfaces. The direction of E, i.e. the axis normal to the crystal plates, was set to be along the $\langle 100\rangle$ or $\langle 111\rangle$ direction. Synchrotron radiation x-ray diffraction data were collected in a transmission geometry using a large cylindrical two-dimensional imaging plate (IP) camera at BL02B1 in the SPring-8 synchrotron radiation facility [28,29]. A high SR energy of 35 keV was adopted so that an x ray with a high transmission ratio penetrates through the crystals and that high-angle diffraction patterns can be observed. The x-ray beam incident to the crystals was 150 μm in diameter. The intensity data recorded on the IP were obtained as the summation of diffraction spots from each domain in the x-ray-irradiated area. The measurement temperature was 25 °C, at which BNT is assumed to have a rhombohedral structure (space group $R3c$) [22]. Recently, Gorfman and Thomas [30] have revealed that BNT at room temperature belongs to space group Cc with a small monoclinic distortion from the $R3c$ symmetry. Since this monoclinic distortion is less than 0.1%, the crystal structure can be regarded to have space group $R3c$ to investigate the overall behavior of the domain dynamics [30,31]. Here, we adopt rhombohedral $R3c$ as the ground-state space group of BNT to simplify the discussion.

First, an E of -100 kV/cm, which was much higher than the coercive field (E_c) of 40–50 kV/cm (shown later), was applied to the crystals (along the $\langle 100\rangle$ or $\langle 111\rangle$ direction) as a poling treatment, and then diffraction patterns of the poled crystals were measured at $E = 0$ kV/cm. Hereafter, this poled state at $E = 0$ kV/cm is called "$-P_r$ state". Next, to investigate the dynamic response of the domain structure during the polarization switching, an E of a varying amplitude (on increasing) antiparallel to the poling direction was applied, and an *ex situ* measurement of the diffraction patterns was performed after the application of E was turned off. The amplitude of the antiparallel E was increased up to $+100$ kV/cm, and the resultant poled state ($+P_r$ state) was also analyzed by the *ex situ* SR-XRD measurement. For each *ex situ* measurement, four x-ray oscillation photographs with an oscillation angle $\Delta\omega$ of 10° were obtained at different angles ω.

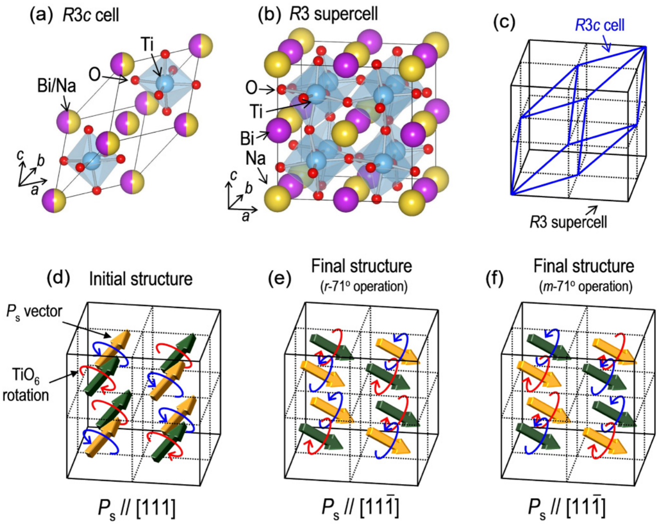

FIG. 1. (Color online) Rhombohedral crystal structures of BNT: (a) the $R3c$ cell with a random distribution of Bi and Na on the A site and (b) the $R3$ supercell with the $\langle 111\rangle$ ordering of Bi and Na. The relationship between these cells is depicted in (c). P_s vectors and rotation directions of the oxygen octahedra in each of the primitive perovskite units in (d) the initial structure (the $R3$ supercell) and in the final structures obtained by the (e) r-71° and (f) m-71° transformation operations [see Table I]. The crystal structures shown in these figures were drawn with the three-dimensional visualization software VESTA (Ref. [51]).

III. METHOD OF CALCULATION

Density functional theory calculations were performed to investigate the behavior of the polarization switching in rhombohedral BNT. The random distribution of Bi and Na on the A site leads to the averaged crystal structure in space group $R3c$ [Fig. 1(a)], while the structure of BNT for the calculations should have a lower symmetry due to an arrangement of Bi and Na [32]. Figure 1(a) shows the $R3c$ cell created from the experimental structural data [22]. First, Bi and Na atoms were arranged on the corner and the body-center A site in the $R3c$ cell, respectively, which corresponds to the $\langle 111\rangle$ ordering of Bi and Na. This structure has an alternate stacking of the Bi-Ti-O and Na-Ti-O blocks along the $\langle 111\rangle$ direction and is equivalent to a supercell of 2 × 2 × 2 perovskite structure [Fig. 1(b)]. This supercell has space group $R3$ because the A-site ordering breaks c-glide symmetry of the $R3c$ structure. The relationship between the $R3c$ cell [Fig. 1(a)] and the $R3$ supercell [Fig. 1(b)] is depicted in Fig. 1(c).

Next, the geometrical optimization (cell volume, cell shape, and atomic positions) was carried out for the $R3$ cell. As a result, the antiphase rotation of the TiO_6 octahedra around the [111] direction, which is seen for the $R3c$ cell, is maintained in the $R3$ cell. Although the geometrical optimization was conducted without a constraint of c-glide symmetry, the atomic positions of oxygen in the $R3$ cell were in good agreement with those in the $R3c$ cell. These differences in the atomic positions were less than 0.005 nm. Figure 1(d) represents the P_s vector of each primitive perovskite unit in the $R3$ cell in which the macroscopic P_s is aligned along the [111] direction. Due to a different structural environment of the A-site atoms, the $R3$ cell has two kinds of the perovskite unit. The P_s vector (dark green) in one unit is directed from Bi to Na, while the P_s vector (bright yellow) in another one is aligned from Na to Bi. The circular arrows in Fig. 1(d) indicate the rotational direction of the TiO_6 octahedra around the $\langle 111\rangle$ direction, which are in antiphase with respect to their adjacent units.

Considering the polarization switching of BNT, three possible mechanisms are considered for the variations of the P_s vectors: two of them are the rotations of the P_s vectors by 71° or 109°, and the remaining one is the direct reversal of the P_s vector by 180°. The energy profiles of the pathways for these three P_s variations from the initial to final states were estimated based on the $R3$ cell as follows. The final crystal structures for the possible mechanisms, i.e. the structures after

TABLE I. Matrices of the transformation operations to obtain the final crystal structures.

Transformation operation	r-71°	m-71°	r-109°	m-109°	r-180°	m-180°
Transformation matrix, M	$\begin{pmatrix}0&1&0\\1&0&0\\0&0&-1\end{pmatrix}$	$\begin{pmatrix}1&0&0\\0&1&0\\0&0&-1\end{pmatrix}$	$\begin{pmatrix}1&0&0\\0&-1&0\\0&0&-1\end{pmatrix}$	$\begin{pmatrix}1&0&0\\0&0&-1\\0&-1&0\end{pmatrix}$	$\begin{pmatrix}0&-1&0\\-1&0&0\\0&0&-1\end{pmatrix}$	$\begin{pmatrix}-1&0&0\\0&-1&0\\0&0&-1\end{pmatrix}$
Direction of P_s in the final structure	$[11\bar{1}]$	$[11\bar{1}]$	$[1\bar{1}\bar{1}]$	$[1\bar{1}\bar{1}]$	$[\bar{1}\bar{1}\bar{1}]$	$[\bar{1}\bar{1}\bar{1}]$

the variation of the P_s vectors by 71°, 109°, and 180°, were created by applying the rotation or mirror-symmetry operation to the initial structure [Figs. 1(b) and 1(d)]. The transformation from the initial to final structure is expressed by

$$\xi_f = M\xi_i, \tag{1}$$

where ξ_i and ξ_f are the atomic positions (coordinates) in the initial and final structures, and M denotes the transformation matrix. Table I lists the transformation matrices (M). Two different operations were made each for the three kinds of the P_s variations (71°, 109°, 180°); one is the rotation operation (denoted by the prefix "r" in Table I) and the other is the mirror-symmetry operation (denoted by the prefix "m"). For example, the final structures of the 71° P_s variations are shown in Figs. 1(e) [the r-71° operation] and 1(f) [the m-71° operation]. Both these two final structures exhibit the same P_s vectors (along the $[11\bar{1}]$ direction) forming an angle of 71° from the initial-P_s vectors (along the [111] direction) [see Fig. 1(d)]. The difference in these final structures arises from their distinct (antiphase) tilting of the TiO_6 octahedra. It should be emphasized that these two final structures [Figs. 1(e) and 1(f)] have a relationship similar to the enantiomers; i.e. they are mirror images of each other and thus have the same structural energies. The two final structures have, however, their distinct pathways from the same initial structure and therefore yield different energy barriers for their respective P_s variations, which is discussed later in detail.

The switching pathway of the P_s variation from the initial to final structure was generated by the following linear interpolation. The fractional coordinates (ξ_λ) of atoms in an intermediate structure were obtained by

$$\xi_\lambda = (1-\lambda)\xi_i + \lambda\xi_f, \tag{2}$$

where λ is the interpolation parameter in the range of $0 \le \lambda \le 1$. For each of the intermediate structures with different λ, the cell shape and volume were optimized in space group $P1$ with the fixed ξ_λ. By plotting the total energies (E_{total}) calculated for the optimized structures with respect to λ, the energy profile along the switching pathway of the P_s variation was obtained each for the six final structures generated by the operations listed in Table I.

The DFT calculations were performed with the generalized gradient approximation [33] using a plane-wave basis set as implemented in the Vienna *ab initio* simulation package (VASP). We used the projector-augmented wave potentials [34] with the valence-electron configurations of $5d^{10}6s^26p^3$ for Bi, $2p^63s^1$ for Na, $3p^63d^24s^2$ for Ti, and $2s^22p^4$ for O. The Perdew-Burke-Ernzerhof functional modified for solids (PBEsol) [35] was employed for the exchange-correlation potential. A plane-wave cutoff energy of 520 eV was adopted, and electronic energy was converged to less than 10^{-5} eV in all calculations. The Monkhorst-Pack k-mesh of 2 × 2 × 2 was adopted for geometrical optimization calculations of the $R3$ cell of BNT [Fig. 1(b)]. The optimizations of the cell shape and volume of the intermediate structures were performed in space group $P1$ in the similar manner.

IV. RESULTS AND DISCUSSION

Figure 2 shows the polarization hysteresis loops measured along the ⟨100⟩ [Fig. 2(a)] and ⟨111⟩ [Fig. 2(b)] directions. The crystals exhibited a remanent polarization (P_r) of 29 μC/cm^2 along the ⟨100⟩ direction and 52 μC/cm^2 along the ⟨111⟩ direction at 25 °C. From the P_s of 55 μC/cm^2 along the ⟨111⟩ direction of BNT [36], the polarization values are estimated to be 32 μC/cm^2 along the ⟨100⟩ direction and 55 μC/cm^2 along the ⟨111⟩ direction, which agree well with the measured P_r values. The amplitude of E for the poling (100 kV/cm) is much higher than the E_c values (40 kV/cm along ⟨100⟩ and 50 kV/cm along ⟨111⟩). These polarization measurements show that the P_s vectors are almost completely aligned along the E directions by the poling treatments, which are found by the SR-XRD observations.

Figure 3 shows the typical diffraction patterns observed for the ⟨100⟩-poled [Fig. 3(a)] and ⟨111⟩-poled [Fig. 3(b)] crystals at $E = 0$ kV/cm. No diffraction pattern originating from gold electrodes or impurities was observed, and all diffraction spots can be indexed in space group $R3c$ with the lattice parameters of $a_h \sim 0.548$ nm and $c_h \sim 1.356$ nm. High-angle diffraction patterns with a maximum $\sin\theta/\lambda$ of ~14.3 nm^{-1} ($d \sim 0.035$ nm) were observed. Among the fundamental $h\ k\ l$ spots attributed to the pseudocubic primitive cell of perovskite ABO_3, 1/2{$o\ o\ o$} spots (o represents odd number) are clearly

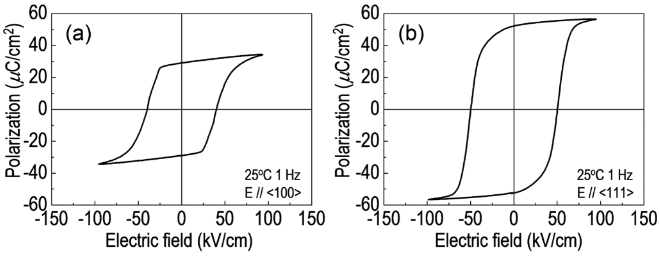

FIG. 2. Polarization hysteresis loops of the BNT single crystals along the (a) ⟨100⟩ and (b) ⟨111⟩ directions.

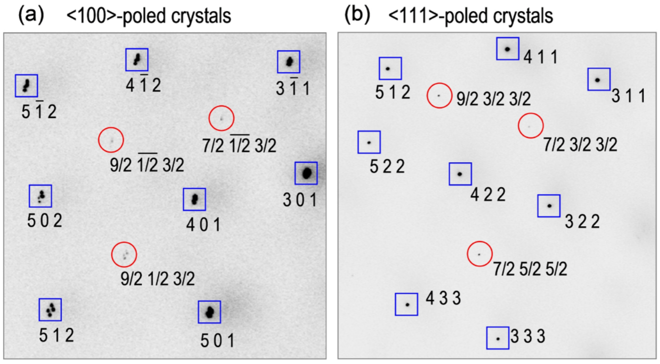

FIG. 3. (Color online) Typical diffraction patterns of (a) ⟨100⟩-poled and (b) ⟨111⟩-poled BNT crystals observed by using the cylindrical two-dimensional imaging plate.

found for both the ⟨100⟩- and ⟨111⟩-poled crystals. The $1/2\{o\ o\ o\}$ spots are derived from the tilting of the $\mathrm{TiO_6}$ octahedra in space group $R3c$ [37].

Figures 4(a) and 4(b) show the 5 1 2 reflections at $E = 0$ kV/cm in the $-P_\mathrm{r}$ state [Fig. 4(a)] and in the $+P_\mathrm{r}$ state [Fig. 4(b)] for the ⟨100⟩-poled crystals recorded in the same IP region. This fundamental reflection is found to exhibit four splitting spots in both the $-P_\mathrm{r}$ and $+P_\mathrm{r}$ states. The four splitting spots are seen not only in the other fundamental $h\ k\ l$ reflections but also in the superlattice $1/2\{o\ o\ o\}$ ones [see Fig. 3(a)]. The splitting of these reflections shows that the poled crystals have a multidomain (MD) structure with the ferroelastic domain walls across which the P_s vectors rotate by 71° or 109°. Figure 4(c) represents the differential intensity map between the $-P_\mathrm{r}$ state (I_minus) in Fig. 4(a) and the $+P_\mathrm{r}$ state (I_plus) in Fig. 4(b). As a result of the polarization switching from the $-P_\mathrm{r}$ state to the $+P_\mathrm{r}$ state, the intensities of two spots became stronger [denoted as "+" in Fig. 4(c)], while those of the other two spots were diminished in intensity [denoted as "−" in Fig. 4(c)], as can be clearly seen in Fig. 4(c).

Here, we discuss the dynamics of the polarization switching by applying E along the ⟨100⟩ direction. Figure 5 shows a model of the polarization switching in the rhombohedral crystal with the P_s vectors along the ⟨111⟩ directions. Eight possible directions of the P_s vectors along the equivalent ⟨111⟩ axes are depicted in Fig. 5(a). The state with all of these P_s vectors corresponds to an unpoled state. When a high E is applied to the unpoled crystals along the $[00\bar{1}]$ direction as the poling treatment, the P_s vectors are aligned, and the resultant state (corresponding to the $-P_\mathrm{r}$ state) is assumed to contain four variants of the energetically equivalent domains with $P_\mathrm{s}//[11\bar{1}]$, $[1\bar{1}\bar{1}]$, $[\bar{1}1\bar{1}]$, and $[\bar{1}\bar{1}\bar{1}]$, as shown in Fig. 5(b). The application of $E//[001]$ to the $[00\bar{1}]$-poled crystals (opposite to the poling direction) leads to a polarization switching and then the $+P_\mathrm{r}$ state with P_s //[111], $[1\bar{1}1]$, $[\bar{1}11]$, and $[\bar{1}\bar{1}1]$ is established [Fig. 5(c)].

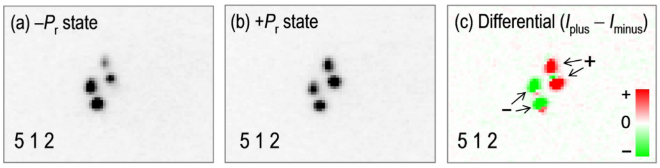

FIG. 4. (Color online) The 512 reflection in the (a) $-P_\mathrm{r}$ and (b) $+P_\mathrm{r}$ states observed for the ⟨100⟩-poled crystals. (c) Differential intensity map between (a) the $-P_\mathrm{r}$ state (I_minus) and (b) the $+P_\mathrm{r}$ state (I_plus). The notations "+" and "−" in (c) indicate the spots exhibiting positive and negative of I_plus-I_minus, respectively.

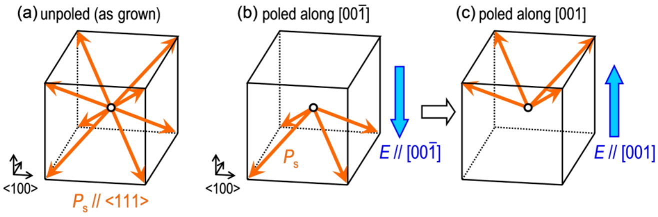

FIG. 5. (Color online) (a) Eight equivalent directions of the P_s vector along the ⟨111⟩ direction in rhombohedral BNT. The P_s vectors are depicted in the poled crystals along the (b) $[00\bar{1}]$ and (c) [001] directions.

The model for the polarization switching induced by E//⟨100⟩ illustrated in Fig. 5 is consistent with the experimental results of the SR-XRD measurements. The four splitting spots observed in the $-P_\mathrm{r}$ and $+P_\mathrm{r}$ states [Figs. 4(a) and 4(b)] result from ferroelastic domains with the four equivalent P_s vectors in the poled states [Figs. 5(b) and 5(c)]. The positions of the four splitting spots in the $-P_\mathrm{r}$ and $+P_\mathrm{r}$ states accorded exactly, as observed in Fig. 4, which can be explained by noting that two domains with the opposite P_s vectors that form an angle of 180° (e.g. P_s//[111] and $[\bar{1}\bar{1}\bar{1}]$) are equivalent in our SR-XRD measurements. In addition, the differential intensity map [Fig. 4(c)] strongly suggests that the non-180° (71° and/or 109°) rotation of the P_s vectors (the non-180° P_s rotation) indeed occurs during the polarization switching because the 180° reversal of the P_s vectors (the 180° P_s reversal) should not change the diffraction pattern including the diffraction intensity.

Figure 6(a) shows the 3 2 2 reflection in the $-P_\mathrm{r}$ state observed for the ⟨111⟩-poled crystals. In contrast to the ⟨100⟩-poled crystals exhibiting the splitting spots, the ⟨111⟩-poled crystals exhibit a single 3 2 2 spot without any satellite. The diffraction pattern without splitting was observed also in the $+P_\mathrm{r}$ state for the ⟨111⟩-poled crystals (not shown). These results demonstrate that the ⟨111⟩-poled crystals have the single-domain (SD) state both in the $-P_\mathrm{r}$ and $+P_\mathrm{r}$ states.

We have also investigated the dynamics of the polarization switching by applying E along the ⟨111⟩ direction, i.e. the

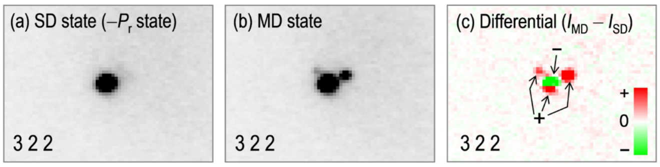

FIG. 6. (Color online) The 322_c reflections in (a) the single-domain (SD) state ($-P_\mathrm{r}$ state) and (b) the multidomain (MD) state of the ⟨111⟩-poled crystals. (c) Differential intensity map between (a) the SD state (I_SD) and (b) the MD state (I_MD). The notations "+" and "−" in (c) indicate the spots exhibiting positive and negative of I_MD-I_SD, respectively.

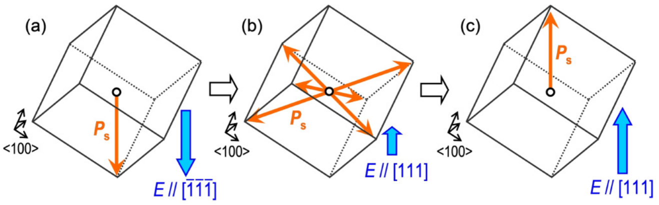

FIG. 7. (Color online) Schematic behavior of the polarization switching under the application of E along the $\langle 111\rangle$ direction: (a) P_s vectors in the SD state poled along the $[\bar{1}\bar{1}\bar{1}]$ direction, (b) intermediate MD state during the P_s reversal, and (c) the SD state poled along the [111] direction.

behavior of the polarization switching from the $-P_r$ state to the $+P_r$ state. Figure 6(b) exhibits the diffraction pattern of the 3 2 2 reflection during the polarization switching. An E around its E_c was applied opposite to the poling direction to create a MD state before this observation. An apparent splitting of the 3 2 2 reflection is found, showing that the MD state with the 71° and/or 109° domains is created on the way toward the $+P_r$ state. A partial polarization switching leads to the MD state, which is the cause of the splitting of the 3 2 2 reflection.

Figure 6(c) represents the differential intensity map between the SD state (I_{SD}) [Fig. 6(a)] and the MD state (I_{MD}) [Fig. 6(b)] of the $\langle 111\rangle$-poled crystals. It is evident that the 3 2 2 reflection in the MD state contains four diffraction spots. One is the central spot that is present also in the SD state with the P_s vector parallel to the poling direction [Fig. 7(a)] and had a decreased diffraction intensity in the MD state [denoted as "$-$" in Fig. 6(c)]. The other three are the satellites attributed to the variant domains [denoted as "+" in Fig. 6(c)] with the three different P_s vectors, as depicted in Fig. 7(b). The 180° P_s reversal does not, indeed, lead to the satellite spots because the switching of the P_s vectors by 180° should have no change in the position of diffraction spot. The three satellite spots observed for the MD state is, therefore, direct evidence that the polarization switching under $E//\langle 111\rangle$ is governed by the non-180° (71° and 109°) P_s rotation, not by the 180° P_s reversal, as shown in Fig. 7. The non-180° P_s rotation during the P_s switching has been reported also for rhombohedral $Pb(Zn_{1/3}Nb_{2/3})O_3$-$PbTiO_3$ single crystals under $E//\langle 111\rangle$ [38,39].

Figure 8 indicates the energy profiles for the 71° [Fig. 8(a)], 109° [Fig. 8(b)], and 180° switching pathways [Fig. 8(c)] of the P_s variations evaluated by the DFT calculations. The labels of the profiles denote the transformation operations (see Table I) used to create the final structures at the interpolation parameter $\lambda = 1.0$. All the energy profiles have bilateral symmetry and a peak at $\lambda = 0.5$. It is suggested that the peak heights in E_{total} at $\lambda = 0.5$ (E_b) are in close relation to the energy barriers for the switching pathways during their respective P_s variations. The differential E_{total} values (per perovskite primitive cell "pc") are listed in Table II along with the details of the crystal structures at $\lambda = 0.0$ (initial), 0.5 (transient), and 1.0 (final). The differential E_{total} value at $\lambda = 0.5$ corresponds to the E_b value for each switching pathway. For the non-180° (71° and 109°) P_s variations, the m operation exhibits a lower E_b compared with the r operation. For the 180° P_s variation, the r-operation pathway has a lower E_b than the m-operation pathway. Comparing the operations resulting in the lower E_b values of their respective P_s variations, the m-71° pathway has the lowest E_b of 0.06 eV/pc.

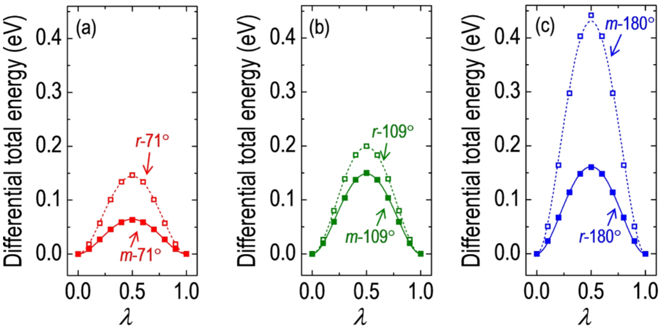

FIG. 8. (Color online) Total energy profiles (per primitive perovskite cell) for the (a) 71°, (b) 109°, and (c) 180° switching pathways as a function of the interpolation parameter λ [see Eq. (2)]. Labels of the curves correspond to the transformation operations listed in Table I for obtaining the final structures at $\lambda = 1.0$.

Here, we discuss the dynamic behavior of the TiO_6 octahedra during the P_s variations. The structure of BNT in space group $R3c$ has the rotation of TiO_6 octahedra around the [111] direction parallel to the P_s vector [Fig. 1(d)]. This octahedral tilt system is denoted as "$a^-a^-a^-$" by the Glazer notation [37], where the superscript "$-$" indicates the antiphase rotation around each crystallographic axis of the $R3$ cell [see Fig. 1(b)]. In the Glazer notation, the repetition of the same letter indicates equality of rotation angles around the rotation axes; i.e. $a^-a^-a^-$ means equal rotations around all three axes, while $a^-b^-c^-$ means three unequal rotations. Hereafter, this rule is ignored to differentiate the rotation symmetries around three axes during the P_s variations. The perovskite structures in which anitiphase rotations exist around all three axes is represented as $a^-b^-c^-$ symmetry whether their rotation angles are equal or not. The tolerance factor $t = (r_A + r_O)/\sqrt{2}(r_B + r_O)$, where r_A, r_B, and r_O are the ionic radii of the A site, B site, and O ions by using Shannon's effective ionic radii [40], is calculated to be 0.977 for BNT [41]. This t value less than 1 indicates that the A-site environment in BNT has an ample space. The TiO_6 octahedra, therefore, rotate so that some O^{2-} ions move close to the A-site cations to result in an energetically favorable environment around the A site [42,43]. The octahedral rotation makes the angle of the Ti-O-Ti bonding apart from 180°. The averaged angle of the Ti-O-Ti bonding ($\omega_{\text{Ti-O-Ti}}$) of the $R3$ cell obtained by the DFT calculations is 156.7°.

The octahedral rotation symmetry of $a^-b^-c^-$ in BNT is transiently changed during the P_s variation. The rotation symmetry and the $\omega_{\text{Ti-O-Ti}}$ of the $R3$ cell at the energetic peak ($\lambda = 0.5$) of each switching pathway are also listed in Table II. The P_s vectors vary along the distinct pathways, which modifies the tilt symmetry from $a^-b^-c^-$ in the ground state to, e.g. $a^0b^0c^-$ for the r-71° operation and to $a^-b^-c^0$ for the m-71° operation in the transient state at $\lambda = 0.5$ (the superscript "0" denotes no rotation around the corresponding axis). The r-71° P_s variation is permitted while maintaining z^- and changes the remaining two symmetries from a^-b^- at $\lambda = 0$, to a^0b^0 at $\lambda = 0.5$. In contrast, the m-71° P_s variation

TABLE II. Characteristic structural parameters in the initial, transient, and final states during the P_s variations.

Structure	Initial structure	Transient structure at $\lambda = 0.5$						Final structure
		r-71°	m-71°	r-109°	m-109°	r-180°	m-180°	
λ(-)[a]	0.0	0.5	0.5	0.5	0.5	0.5	0.5	1.0
Differential E_{total} (eV/pc)	0.00	0.14	0.06	0.20	0.15	0.16	0.43	0.00
$\omega_{\text{Ti-O-Ti}}$ (deg.)[b]	156.7	163.6	157.6	164.6	157.4	158.2	180.0	156.7
Space group	$R3$	$C2$	Cm	$C2$	Cm	$R3_2$	$R\bar{3}m$	$R3$
Octahedral tilt system[c]	$a^-b^-c^-$	$a^0b^0c^-$	$a^-b^-c^0$	$a^-b^0c^0$	$a^0b^-c^-$	$a^-b^-c^-$	$a^0b^0c^0$	$a^-b^-c^-$
Direction of P_s	[111]	[110]	[110]	[100]	[100]	($P_s = 0$)	($P_s = 0$)	[d]

[a] Interpolation parameter in Eq. (2).

[b] Averaged angle of the Ti-O-Ti bonding.

[c] Tilt system is denoted in a manner similar to the Glazer notation (see text).

[d] The direction of P_s in the final structure depends on the switching pathway (see Table I).

alters the symmetry from c^- at $\lambda = 0$ to c^0 at $\lambda = 0.5$ while maintaining a^-b^-. For the m-71° variation, the $\omega_{\text{Ti-O-Ti}}$ of 157.6° in the transition structure is almost the same as that of 156.7° in the initial structure ($\lambda = 0$), whereas the r-71° variation remarkably increases $\omega_{\text{Ti-O-Ti}}$ to 163.6° at $\lambda = 0.5$. For the r-71° P_s variation, the ground-state structure with $\omega_{\text{Ti-O-Ti}}$ of 156.7° is largely distorted associated with an energy cost in the transition state at $\lambda = 0.5$. The lower E_b of the m-71° pathway is found to originate from the unchanged $\omega_{\text{Ti-O-Ti}}$ during its P_s variation.

The discussion of the rotation symmetry described above has no relation to the configuration of Bi and Na on the A site and therefore are valid for BNT with space group $R3c$. It is reasonable to consider that the m-71° P_s variation with the unchanged $\omega_{\text{Ti-O-Ti}}$ during the polarization switching leads to a low-E_b pathway in the BNT crystals, as also discussed in the structural calculations of BiFeO$_3$ in space group $R3c$ [44].

In reality, a polarization switching in ferroelectric crystals proceeds via nucleation and growth of domains. The results of the SR-XRD measurements clearly show that the P_s switching is governed by the nucleation and growth of 71° and/or 109° domains. According to the phenomenological LGD theory, the formation energy of the planer domain wall (E_{DW}) is expressed by

$$E_{\text{DW}} = \tfrac{2}{3}|\Delta \mathbf{P}_s|\sqrt{2gE_b}, \tag{3}$$

where $\Delta \mathbf{P}_s$ is the differential vector of P_s between the two adjacent domains, and g is the gradient coefficient along the axis perpendicular to the DW (see Appendix). The $|\Delta \mathbf{P}_s|$ value becomes larger as the angle of the P_s variation across the DW increases; i.e. $|\Delta \mathbf{P}_s| = P_s \times (2/\sqrt{3})$ for the 71° DW, $P_s \times (2\sqrt{2}/\sqrt{3})$ for the 109° DW, and $P_s \times 2$ for the 180° DW. Since the g values of BNT have not been reported as far as we know, the g values of rhombohedral ($R3m$) BaTiO$_3$ (BT) [45] are used in our calculations of E_{DW}: $g = 2.0$ (71° DW), 2.0 (109° DW), and 18.3 (180° DW//[1$\bar{1}$0]) in a unit of $10^{-11}\,\text{J}\cdot\text{m}^3/\text{C}^2$. From these g values, the P_s of 55 μC/cm^2, the pc volume of 5.8×10^{-29} m^3, and the lower E_b between the r and m pathways of each P_s variation, the E_{DW} values are estimated to be 36 mJ/m^2 (the 71° DW), 76 mJ/m^2 (the 109° DW), and 290 mJ/m^2 (the 180° DW). The E_{DW} of the 71° DW is approximately half that of the 109° DW and an eighth that of the 180° DW. These DFT calculations show that the P_s switching in BNT proceeds through the nucleation and growth of the 71° domains, which is consistent with the SR-XRD measurements.

These E_{DW} values of BNT are much larger than those of rhombohedral BT obtained by the LGD calculations [45]: $E_{71^\circ\text{DW}} = 3.7$ mJ/m^2, $E_{109^\circ\text{DW}} = 7.8$ mJ/m^2, $E_{180^\circ\text{DW}} = 36$ mJ/m^2, which can be explained by taking the difference in E_c into account. The E_c of the BNT crystals [40 kV/cm; see Fig. 2(a)] is higher by approximately one order of magnitude than that of rhombohedral BT single crystals at -100°C ($E_c \sim 1$ kV/cm) [46]. The E_{DW} values of BNT obtained in this study are comparable with those recently reported for BiFeO$_3$ ($E_{71^\circ\text{DW}} = 130$–170 mJ/m^2, $E_{109^\circ\text{DW}} = 30$–60 mJ/m^2, $E_{180^\circ\text{DW}} = 80$–100 mJ/m^2) [47,48]. It is worth noting that BiFeO$_3$ has a rhombohedral $R3c$ structure, as BNT has, and that BiFeO$_3$ single crystals exhibit an E_c of 30–50 kV/cm [49]. This E_c is close to that of the BNT crystals (40–50 kV/cm).

The SR-XRD measurements in this study reveal that the non-180° P_s rotation is dominant in the polarization switching in both cases of E along the $\langle 100\rangle$ and $\langle 111\rangle$ directions. Our DFT calculations show that the m-71° P_s variation provides the energetically favorable pathway. We therefore conclude that the polarization switching is achieved via the 71° P_s rotation in the BNT single crystals.

V. CONCLUSIONS

The P_s switching behavior has been investigated for the high-quality single crystals of BNT with an E along the $\langle 100\rangle$ and $\langle 111\rangle$ directions by using high-energy SR-XRD measurements. The SR-XRD diffraction analyses provide the direct evidence that the P_s switching is governed by the non-180° P_s variation. The DFT calculations, in which the octahedral tilts with different P_s pathways during the polarization switching are taken into account, strongly suggest that the 71° P_s variation is more energetically favorable than the 109° and 180° P_s variations. Our SR-XRD analyses and DFT calculations lead to the conclusion that the E-induced polarization switching is governed by the 71° P_s rotation in the BNT crystals.

ACKNOWLEDGMENTS

This research is supported by a Grant-in-Aid for Research Fellows of the Japan Society for the Promotion of Science

(JSPS; No. 11J06837). The SR experiments were carried out with the approval of the Japan Synchrotron Radiation Research Institute (JASRI; Proposal Nos. 2011B1386, 2012A1359, and 2012B1243). This research is partly granted by JSPS through the Funding Program for Next Generation World-Leading Researchers (NEXT Program), initiated by the Council for Science and Technology Policy (CSTP).

APPENDIX

Here, we describe the methodology of the calculation of the domain wall (DW) energy based on the Landau-Ginzburg-Devonshire (LGD) theory, which follows the procedure proposed in Ref. [45]. Let us consider a single planer DW in a perfect crystal, across which the vector of polarization ($\mathbf{P}$) gradually varies from one P_s state to the other. The P_s vectors ($\mathbf{P}_s$) in the two domains at a sufficient distance from the DW are denoted as $\mathbf{P}_{s0}$ and $\mathbf{P}_{s1}$ which are directed to the $\langle 111 \rangle$ direction in rhombohedral $(Bi_{0.5}Na_{0.5})TiO_3$ (BNT). The DW is assumed to be electrically neutral (uncharged) and free of stress, which is determined by the continuity of P_s and the compatibility of spontaneous strain across the DW.

Here, the orthogonal x, y, and z axes are introduced as follows. First, the x axis is determined to be perpendicular to the planer DW. The electrical neutrality of the DW imposes the condition that the DW is placed parallel to $\Delta\mathbf{P}_s = \mathbf{P}_{s1} - \mathbf{P}_{s0}$, which is the differential vector of P_s in the two adjacent domains [50]. Here, the y axis is defined as the direction of $\Delta\mathbf{P}_s$, which is perpendicular to the x axis. Finally, the z axis is determined to be the third orthogonal axis perpendicular to both the x and y axes. In this orthogonal system, the $\mathbf{P}_{s0}$ and $\mathbf{P}_{s1}$ vectors are denoted as $\mathbf{P}_{s0} = (p_{sx}, -p_{sy}, p_{sz})$ and $\mathbf{P}_{s1} = (p_{sx}, p_{sy}, p_{sz})$, where the P_s components of p_{sx}, p_{sy}, and p_{sz} are determined by the kind of the DW (71°, 109°, and 180°) and by the orientation of the DW. The DW geometry perpendicular to the x axis implies that the polarization varies only along the x axis and is constant in the y-z plane; the coordinate-dependent $\mathbf{P}$ variation in the domain structure is represented as $\mathbf{P}(x,y,z) = \mathbf{P}(x) = [p_x(x), p_y(x), p_z(x)]$.

The total free energy G_{total} of the crystal containing a DW is expressed by

$$G_{\text{total}} = \iiint (f_L + f_{\text{el}} + f_{\text{dep}} + f_{\text{grad}})\,dx\,dy\,dz \tag{A1}$$

where f_L is the free energy density based on the Landau potential, f_{el} is the elastic and electrostriction energy density due to the local strain, f_{dep} is the electrostatic energy density due to the depolarization field, and f_{grad} is the Ginzburg gradient energy density depending on the spatial derivatives of $\mathbf{P}$ ($\partial\mathbf{P}/\partial x$). Even if the DW has an electrical neutrality, a small amount of local electric charge is possibly present in the vicinity of the DW, making a certain contribution of the f_{dep} to the G_{total}. To simplify the discussion in this study, the local charge is assumed to be negligible in the whole domain structures. In this assumption, f_{dep} is excluded in Eq. (A1).

The assumption of zero local charge, i.e. $\nabla \cdot \mathbf{P}(x) = 0$ leads to the constraint that the x component of the $\mathbf{P}$ vector p_x is constant ($\partial p_x/\partial x = 0$). In addition, the trajectory of $\mathbf{P}(x)$ can be assumed to represent a straight line from $\mathbf{P}_{s0}$ [$= \mathbf{P}(-\infty)$] to $\mathbf{P}_{s1}$ [$= \mathbf{P}(+\infty)$]; i.e. $\mathbf{P}(x)$ is denoted as

$$\begin{aligned}\mathbf{P}(x) &= [1 - \lambda^*(x)]\mathbf{P}_{s0} + \lambda^*(x)\mathbf{P}_{s1}\\ &= \{p_{sx}, [2\lambda^*(x) - 1]p_{sy}, p_{sz}\},\end{aligned} \tag{A2}$$

where $\lambda^*(x)$ is the fractional parameter depending only on the coordinate x. The boundary conditions of $\mathbf{P}$ [$\mathbf{P}(-\infty) = \mathbf{P}_{s0}$ and $\mathbf{P}(+\infty) = \mathbf{P}_{s1}$] are represented by $\lambda^*(-\infty) = 0$ and $\lambda^*(+\infty) = 1$. As can be seen in Eq. (A2), the assumption of the straight polarization trajectory indicates the constant p_z component ($= p_{sz}$), and thus only the p_y component varies along the x axis. As a result, the DWs considered here are the Ising-type ($\partial p_z/\partial x = 0$), not the Bloch-type ($\partial p_z/\partial x \neq 0$). The LGD calculations by Marton *et al.* [45] show that the DW energies with and without the assumption of $\nabla \cdot \mathbf{P}(x) = 0$ show a small difference less than 10% for rhombohedral ferroelectrics (71°, 109°, 180° DWs).

The Landau-potential term f_L considered here is expanded up to fourth order in the polar components (p_x, p_y, p_z) in the orthogonal symmetry. As is often discussed, the f_{el} term in the single-domain (homogeneous) state can be added into the f_L term through the renormalization of its expansion coefficients, when minimizing the free energy with respect to the lattice strain. As a result, the collected local energy term $f_{\text{local}} = f_L + f_{\text{el}}$ can be represented as a fourth-order function of the polar components. In addition, due to the linear relationship between $\mathbf{P}$ and λ^* [Eq. (A2)], the f_{local} can be expanded also in λ^* as a fourth-order function. Considering the boundary condition that the f_{local} exhibits a minimum energy at $P_y = \pm P_{sy}$ ($\lambda = 0$ and 1), the f_{local} can be expressed as

$$\begin{aligned}f_{\text{local}} &= f_0 + E_b^*\left\{1 - \left[\frac{p_y(x)}{p_{sy}}\right]^2\right\}^2\\ &= f_0 + 16E_b^*\lambda^*(x)^2[1 - \lambda^*(x)]^2,\end{aligned} \tag{A3}$$

where f_0 is the minimum local energy density corresponding to the ground state of the single-domain crystals, and E_b^* is the barrier height of f_{local} at $p_y = 0$ ($\lambda^* = 0.5$). Noting that p_y is the only variable component of $\mathbf{P}$ and varies only along the x axis, the Ginzburg gradient factor f_{grad} is described as

$$f_{\text{grad}} = \frac{1}{2}g\left(\frac{dp_y}{dx}\right)^2 = 2gp_{sy}^2\left(\frac{d\lambda^*}{dx}\right)^2, \tag{A4}$$

where g is the gradient coefficient that depends on the geometry of DW. The domain wall energy E_{DW} per unit DW area (A_{DW}) can be obtained as

$$E_{\text{DW}} = \frac{G_{\text{total}} - G_0}{A_{\text{DW}}} = \int_{-\infty}^{+\infty} (f_{\text{local}} + f_{\text{grad}} - f_0)\,dx. \tag{A5}$$

The $\lambda(x)$ giving the minimum E_{DW} is found by solving the Euler-Lagrange equation

$$\frac{\partial f_{\text{local}}}{\partial \lambda^*} - \frac{d}{dx}\left[\frac{\partial f_{\text{grad}}}{\partial\left(\frac{d\lambda^*}{dx}\right)}\right] = 0. \tag{A6}$$

As is well known for the LGD model with f_{grad}, this solution provides the $\lambda(x)$ with the hyperbolic function as follows:

$$\lambda^*(x) = \frac{1}{2}\tanh\left(\frac{x}{\delta_{\text{DW}}}\right) + \frac{1}{2}, \tag{A7}$$

$$p_y(x) = p_{sy}\tanh\left(\frac{x}{\delta_{\text{DW}}}\right), \tag{A8}$$

where $\delta_{\text{DW}} = p_{sy}\sqrt{g/(2E_b^*)}$ is a parameter related to the DW width. The domain wall energy E_{DW} can be obtained by substituting Eqs. (A3) and (A4) into Eq. (A5)

$$E_{\text{DW}} = \tfrac{4}{3}p_{sy}\sqrt{2gE_b^*} = \tfrac{2}{3}|\Delta\mathbf{P}_s|\sqrt{2gE_b^*}. \tag{A9}$$

For estimating E_{DW} for BNT in this study, the E_b value obtained by density functional theory calculations is adopted as the E_b^* value; i.e. the f_{local} as a function of $\mathbf{P}(\lambda^*)$ [Eq. (A2)] is approximated by the E_{total} as a function of $\xi(\lambda)$ [Eq. (2)].

[1] L. M. Eng, Nanotechnology **10**, 405 (1999).

[2] J. Fousek, D. B. Litvin, and L. E. Cross, J. Phys.: Condens. Matter **13**, L33 (2001).

[3] S. Wada, S. Suzuki, T. Noma, T. Suzuki, M. Osada, M. Kakihana, S.-E. Park, L. E. Cross, and T. R. Shrout, Jpn. J. Appl. Phys. **38**, 5505 (1999).

[4] T. Sluka, A. K. Tagantsev, D. Damjanovic, M. Gureev, and N. Setter, Nat. Commun. **3**, 748 (2012).

[5] S. Y. Yang, J. Seidel, S. J. Byrnes, P. Shafer, C.-H. Yang, M. D. Rossell, P. Yu, Y.-H. Chu, J. F. Scott, J. W. Ager, L. W. Martin, and R. Ramesh, Nat. Nanotechnol. **5**, 143 (2010).

[6] J. Seidel, D. Fu, S.-Y. Yang, E. Alarcón-Lladó, J. Wu, R. Ramesh, and J. W. Ager, Phys. Rev. Lett. **107**, 126805 (2011).

[7] A. Pramanick, A. D. Prewitt, J. S. Forrester, and J. L. Jones, Crit. Rev. Solid State Mater. Sci. **37**, 243 (2012).

[8] G. Catalan, J. Seidel, R. Ramesh, and J. F. Scott, Rev. Mod. Phys. **84**, 119 (2012).

[9] C.-L. Jia, S.-B. Mi, K. Urban, I. Vrejoiu, M. Alexe, and D. Hesse, Nat. Mater. **7**, 57 (2008).

[10] L. Hong, A. Soh, Q. Du, and J. Li, Phys. Rev. B **77**, 094104 (2008).

[11] C. T. Nelson, P. Gao, J. R. Jokisaari, C. Heikes, C. Adamo, A. Melville, S.-H. Baek, C. M. Folkman, B. Winchester, Y. Gu, Y. Liu, K. Zhang, E. Wang, J. Li, L.-Q. Chen, C.-B. Eom, D. G. Schlom, and X. Pan, Science **334**, 968 (2011).

[12] A. P. Levanyuk and D. G. Sannikov, Sov. Phys. Uspekhi **17**, 199 (1974).

[13] Y. Ishibashi and Y. Takagi, Jpn. J. Appl. Phys. **15**, 1621 (1976).

[14] E. Bousquet, M. Dawber, N. Stucki, C. Lichtensteiger, P. Hermet, S. Gariglio, J.-M. Triscone, and P. Ghosez, Nature **452**, 732 (2008).

[15] N. A. Benedek and C. J. Fennie, J. Phys. Chem. C **117**, 13339 (2013).

[16] R. E. Newnham, R. W. Wolfe, and J. F. Dorrian, Mater. Res. Bull. **6**, 1029 (1971).

[17] Y. Noguchi, T. Goto, M. Miyayama, A. Hoshikawa, and T. Kamiyama, J. Electroceramics **21**, 49 (2008).

[18] C. Fennie and K. Rabe, Phys. Rev. B **72**, 100103 (2005).

[19] D. Meier, J. Seidel, A. Cano, K. Delaney, Y. Kumagai, M. Mostovoy, N. A. Spaldin, R. Ramesh, and M. Fiebig, Nat. Mater. **11**, 284 (2012).

[20] R. Eitel and C. Randall, Phys. Rev. B **75**, 094106 (2007).

[21] G. A. Smolensky, V. A. Isupov, A. I. Agranovskaya, and N. N. Krainik, Sov. Phys. Solid State **2**, 2651 (1961).

[22] G. O. Jones and P. A. Thomas, Acta Crystallogr. Sect. B Struct. Sci. **58**, 168 (2002).

[23] K. Yamamoto, M. Suzuki, Y. Noguchi, and M. Miyayama, Jpn. J. Appl. Phys. **47**, 7623 (2008).

[24] Y. Kitanaka, H. Onozuka, Y. Noguchi, and M. Miyayama, Ferroelectrics **414**, 24 (2011).

[25] K. Yamamoto, Y. Kitanaka, M. Suzuki, M. Miyayama, Y. Noguchi, C. Moriyoshi, and Y. Kuroiwa, Appl. Phys. Lett. **91**, 162909 (2007).

[26] Y. Kitanaka, Y. Noguchi, and M. Miyayama, Jpn. J. Appl. Phys. **49**, 09MC06 (2010).

[27] Y. Kitanaka, Y. Noguchi, and M. Miyayama, Phys. Rev. B **81**, 094114 (2010).

[28] K. Sugimoto, H. Ohsumi, S. Aoyagi, E. Nishibori, C. Moriyoshi, Y. Kuroiwa, H. Sawa, and M. Takata, AIP Conf. Proc. **1234**, 887 (2010).

[29] C. Moriyoshi, S. Hiramoto, H. Ohkubo, Y. Kuroiwa, H. Osawa, K. Sugimoto, S. Kimura, M. Takata, Y. Kitanaka, Y. Noguchi, and M. Miyayama, Jpn. J. Appl. Phys. **50**, 09NE05 (2011).

[30] S. Gorfman and P. A. Thomas, J. Appl. Crystallogr. **43**, 1409 (2010).

[31] D. S. Keeble, E. R. Barney, D. A. Keen, M. G. Tucker, J. Kreisel, and P. A. Thomas, Adv. Funct. Mater. **23**, 185 (2013).

[32] M. Gröting, S. Hayn, and K. Albe, J. Solid State Chem. **184**, 2041 (2011).

[33] D. C. Langreth and J. P. Perdew, Phys. Rev. B **21**, 5469 (1980).

[34] P. E. Blöchl, Phys. Rev. B **50**, 17953 (1994).

[35] J. Perdew, A. Ruzsinszky, G. Csonka, O. Vydrov, G. Scuseria, L. Constantin, X. Zhou, and K. Burke, Phys. Rev. Lett. **100**, 136406 (2008).

[36] M. Suzuki, A. Morishita, Y. Kitanaka, Y. Noguchi, and M. Miyayama, Jpn. J. Appl. Phys. **49**, 09MD09 (2010).

[37] A. M. Glazer, Acta Crystallogr. Sect. A **31**, 756 (1975).

[38] J. Yin and W. Cao, Appl. Phys. Lett. **79**, 4556 (2001).

[39] J. E. Daniels, T. R. Finlayson, M. Davis, D. Damjanovic, A. J. Studer, M. Hoffman, and J. L. Jones, J. Appl. Phys. **101**, 104108 (2007).

[40] R. D. Shannon, Acta Crystallogr. Sect. A **32**, 751 (1976).

[41] Y. Hiruma, H. Nagata, and T. Takenaka, Appl. Phys. Lett. **95**, 052903 (2009).

[42] P. M. Woodward, Acta Crystallogr. Sect. B Struct. Sci. **53**, 32 (1997).

[43] P. M. Woodward, Acta Crystallogr. Sect. B Struct. Sci. **53**, 44 (1997).

[44] A. Lubk, S. Gemming, and N. Spaldin, Phys. Rev. B **80**, 104110 (2009).

[45] P. Marton, I. Rychetsky, and J. Hlinka, Phys. Rev. B **81**, 144125 (2010).

[46] H. H. Wieder, J. Appl. Phys. **26**, 1479 (1955).

[47] O. Diéguez, P. Aguado-Puente, J. Junquera, and J. Íñiguez, Phys. Rev. B **87**, 024102 (2013).

[48] Y. Wang, C. Nelson, A. Melville, B. Winchester, S. Shang, Z. Liu, D. G. Schlom, X. Pan, and L. Chen, Phys. Rev. Lett. **110**, 267601 (2013).

[49] Y. Yoneda, Y. Kitanaka, Y. Noguchi, and M. Miyayama, Phys. Rev. B **86**, 184112 (2012).

[50] J. Fousek and V. Janovec, J. Appl. Phys. **40**, 135 (1969).

[51] K. Momma and F. Izumi, J. Appl. Crystallogr. **41**, 653 (2008).